Bubble deformations and segmented flows in corrugated microchannels at large capillary numbers

Martin Sauzade and Thomas Cubaud*
Department of Mechanical Engineering, Stony Brook University, New York 11794-2300, USA

(Received 10 October 2017; published 28 March 2018)

We experimentally investigate the interaction between individual bubble deformations and collective distortions of segmented flows in nonlinear microfluidic geometries. Using highly viscous carrier fluids, we study the evolution of monodisperse trains of gas bubbles from a square to a smoothly corrugated microchannel characterized with a series of extensions and constrictions along the flow path. The hysteresis in the bubble shape between accelerating and decelerating flow fields is shown to increase with the capillary number. Measurements of instantaneous bubble velocities reveal the presence of a capillary pull that produces a nonmonotonic behavior for the front velocity in accelerating flow regions. Functional relationships are developed for predicting the morphology and dynamics of viscous multiphase flow patterns at the pore scale.

DOI: 10.1103/PhysRevFluids.3.034202

I. INTRODUCTION

Multiphase transport in natural environments often involves the flow of dispersed fluids through irregular passages, including porous, fissured, and fractured media during flooding recovery of oil and gas [1–4], obstructed pulmonary airways during respiration [5], soft mud and sediments tunnels during seabed bioturbation, as well as large-scale geysers and volcanic conduits [6]. In these systems, local heterogeneities in composition and structure of flow paths can lead to complex multifluid phenomena, such as dynamic wetting and adhesion at the walls, coalescence, snap-off, or phase immobilization in capillary traps [7]. Interactions between phase distribution and local geometries can also result in widely disparate residence times of fluid or solid particulates advected through multiscale systems. In addition to local flow geometries, complex fluid composition introduces a range of bulk and interfacial behaviors depending on phase concentration and fluid properties such as solubility, surface tension, density, or viscosity. These complexities have limited the development of technology for the precise flow management of viscous dispersions at the small scale, which requires a better understanding of the combined roles of fluid properties, flow parameters, and confinement of multiphase phenomena.

Miniaturized flow laboratories provide controlled model environments to probe complex dynamic interactions between multiphase arrangements and microgeometries. Examples of flow coupling between suspended particulates and local structures include the lateral displacement of nondeformable spherical particles passing through an assembly of posts in plane microchannels [8], the use of wells and bypass microchannels to capture and release droplets [9], as well as interconnected channels for bubble manipulation [10]. The role of confinement on the shape and stability of individual gas bubbles mobilized in tubes and ducts has been investigated in circular and polygonal capillaries [11,12], constrictions [13,14], and wavy channels [15,16], as well as occluded rectangular conduits [17]. Recently, microfluidic platforms have enabled the advanced manipulation of multiphase flows

*Author to whom correspondence should be addressed: thomas.cubaud@stonybrook.edu

with the capability of generating arrays of monodisperse bubbles and droplets in diverse geometries using a variety of injection schemes and designs [18,19]. The fine-tuning of microfluidic segmented flows opens up new opportunities for systematic model studies of multiphase flows passing through complex paths in porouslike media. Basic geometric elements of microfluidic systems include parallel flow configurations with rectangular channels, which are advantageous for enhancing phase exchange [20], separating flows with branching channels for droplet breakup [21] or phase sorting [22], as well as extensional flows with diverging and converging channels for fluid diagnostics [23] and local alteration of phase arrangements [24]. Among the list of basic microfluidic designs, smoothly corrugated microchannels provide a simple example of nonlinear geometries that can strongly distort bubble shape and motion [25].

In the presence of a highly viscous carrier phase, bubbles significantly deform and adopt a shape that tends to conform to the spatial distribution and magnitude of the surrounding flow field. By contrast, in the case of a low-viscosity continuous phase, bubbles assume smoothly curved end caps, which are typically modeled with spherical caps at low capillary numbers. In parallel flow situations, a lubricating layer between the wall and bubble is known to grow with the capillary number and bubble end caps experience a loss in sphericity due to relatively weaker capillary stresses at the fluid interface. While the bullet shape of deformable fluid elements has been investigated in straight channels [26], relatively less is known about bubble morphology and interaction at large capillary numbers in nonparallel flow configurations, which are characteristic of natural oil flow paths in fissured and porous media. In addition to the need for clarifying the role of convective acceleration on the stability of thick dispersions in porous media, a fundamental challenge consists in relating individual bubble dynamics at the pore scale with macroscopic multiphase flow behavior as a function of phase concentration.

In this article, we experimentally study the transport of bubble trains suspended in high-viscosity oils passing through a series of microfluidic extensions and contractions. In particular, we examine the interactions between multiphase flow arrangements and bubble deformations in nonlinear geometries from moderate to large capillary numbers at low Reynolds numbers $\mathrm{Re} < 10^{-1}$. Bubbles are generated using an elementary hydrodynamic focusing section to produce uniform segmented flows in a square channel. Further downstream, the square channel is connected to a corrugated channel characterized with a smooth modulation of the flow velocity over fixed spatial periods to probe the influence of microfluidic extensional flows on the deformation and compaction of capillary objects in highly viscous liquids. While in parallel flow configurations segmented flows are typically characterized with a constant bubble length, spacing, and velocity, these quantities are shown to significantly vary and produce regularly distorted multiphase arrangements in nonlinear geometries.

II. EXPERIMENTAL METHODS

The microchannel module consists of a 250-μm silicon layer, which is partially etched using deep reactive ion etching, and enclosed between two transparent borosilicate glass slides using anodic bonding techniques to seal the channel [27]. The module is placed on top of an inverted microscope equipped with a high-speed camera to capture large time- and space-resolution movies of bubble dynamics. Regions of flow interest correspond to microchannel areas where the silicon layer is etched through to produce a constant channel height $h = 250\,\mu$m and provide clear optical access. Conventional silicone oils of kinematic viscosity $\nu = 10$ or 10^3 cS are injected into the device using high-pressure syringe pumps to examine the influence of both small and large capillary numbers $\mathrm{Ca} = \eta V_\mathrm{A}/\gamma$, where the dynamic viscosity is $\eta = \rho\nu$, with ρ being the oil density, γ the surface tension, and V_A the average bubble velocity in a corrugation, which is calculated according to $V_\mathrm{A} = \lambda/T$, where λ is the pore length and T is the average period of bubble transport across each pore (Fig. 1). Gas is injected from an air or a CO_2 pressurized cylinder, the flow rate of which is monitored with mass flow meters. Since measurement of small gas flow rates at large pressure is limited, the flow rate is estimated from optical flow measurement similar to previous work in this regime [20]. To produce segmented microfluidic flows, we employ a hydrodynamic focusing section

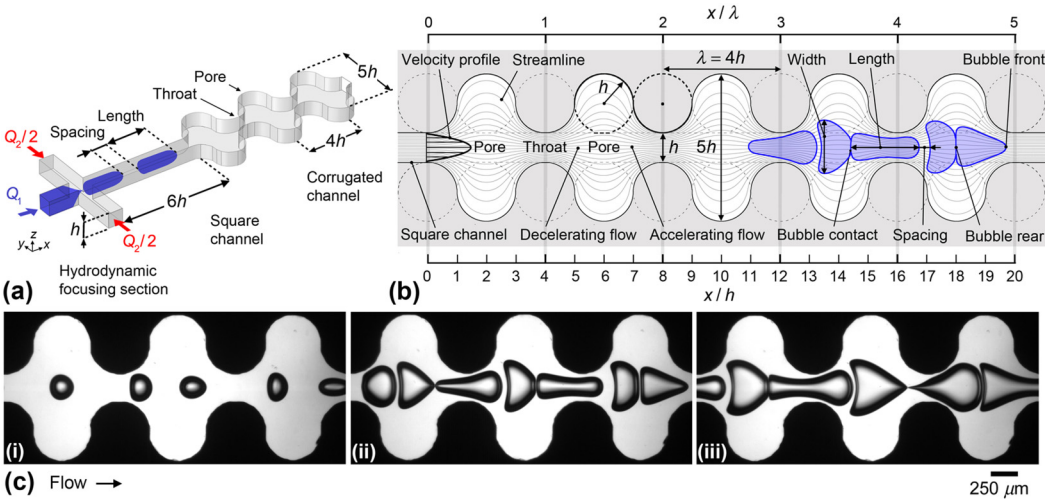

FIG. 1. Segmented flows in corrugated microchannels. (a) Schematics of microfluidic module with focusing section where bubbles are regularly generated in a square channel connected to a corrugated channel. (b) Geometrical detail of corrugated channels made with disks of radius h equally disposed along the square microchannel. (c) Examples of micrographs showing distorted arrangements of air bubbles in viscous silicone oil ($\nu = 10^3$ cS) from dilute flows with small bubbles to concentrated flows with large bubbles: (i) Ca $\approx 3.8 \times 10^{-1}$, (ii) Ca $\approx 2.3 \times 10^{-1}$, and (iii) Ca $\approx 9.9 \times 10^{-1}$.

composed of straight and square microchannels where the gas is introduced in the central channel at volumetric flow rate Q_1 and the liquid is symmetrically injected from the side channels at a total volume flow rate Q_2 [Fig. 1(a)]. Further downstream, the square channel is smoothly connected to a corrugated channel for flow diagnostics. While the initial bubble velocity in the square channel remains constant and scales as $V_0 \approx (Q_1 + Q_2)/h^2$, front and rear bubble velocities decrease in a corrugation and the resulting average bubble velocity in this region is shown to scale as $V_A \approx V_0/2$ in Sec. VI. As the natural time scale of bubble deformation corresponds to $T_C \approx \eta d/\gamma$, with d being the typical bubble size, which is on the order of λ, the capillary number represents the ratio between capillary and convective time scales $\mathrm{Ca} = \eta V_A/\gamma \approx T_C/T$. Therefore, short convective time scales strongly influence bubble behavior at large capillary numbers.

A detailed schematic of the corrugated channel is displayed in Fig. 1(b) and consists of the original square microchannel of height h where equally spaced disks of radius h are alternatively disposed on each side of the main duct. As a result, the wavelength of corrugation is $\lambda = 4h$ and the width of constriction is h while the maximum width of a chamber is $W_{C,MAX} = 5h$. Since such a design is reminiscent of a porous media, we adopt the terminology of throats for constrictions and interstitial pores for expansions. The central plane streamlines associated with a single-phase creeping flow are inscribed in the design for indication of the flow field across the periodic microstructure. Examples of bubble contours in a segmented flow at large Ca have also been superimposed to the drawing to represent the periodically evolving bubble length d, width w, and spacing L in the microchannel. When a train of bubbles passes through such flow geometries, bubbles larger than the flow structure are widely deformed and can form arrays suggesting that of a fish bone structure with large longitudinal and lateral deformations [Fig. 1(c)].

III. SEGMENTED FLOWS IN PARALLEL AND CORRUGATED CONFIGURATIONS

The use of a hydrodynamic focusing section allows for the generation of specific bubble trains. For relatively low capillary numbers Ca $\approx 10^{-2}$, such a flow contactor continuously dispenses elongated bubbles of spacing L_0 and size $d_0 \approx hk/a_2$, where the constant k is close to unity for square channels

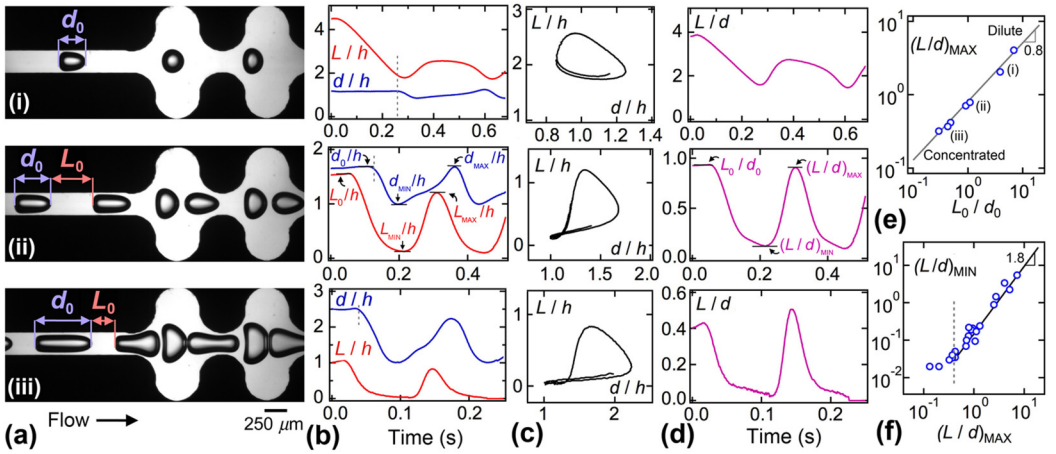

FIG. 2. Morphological evolution of dilute and concentrated segmented flows from straight to corrugated channels. (a) Micrographs of microfluidic multiphase flows with capillary number (i) $\mathrm{Ca} \approx 1.3 \times 10^{-1}$, (ii) $\mathrm{Ca} = 1.9 \times 10^{-1}$, and (iii) $\mathrm{Ca} = 3.3 \times 10^{-1}$. (b) Temporal evolution of bubbles length d/h and spacing L/h at the transition between square and corrugated channels, dashed lines correspond to $x/h = 0$ for the reference bubble front. (c) Relationship between normalized droplet spacing L/h and length d/h in corrugated channel describing orbitals. (d) Temporal evolution of spacing-to-length ratio L/d. (e) Relationship between maximal spacing-to-length ratio in corrugation and square channel, solid line: $(L/d)_{\mathrm{MAX}} = 0.81(L_0/d_0)^{0.8}$. (f) Evolution of minimum ratio $(L/d)_{\mathrm{MIN}}$ with maximum ratio $(L/d)_{\mathrm{MAX}}$, solid line $(L/d)_{\mathrm{MIN}} = 0.15(L/d)^{1.8}_{\mathrm{MAX}}$, dashed line $(L/d)_{\mathrm{MAX}} = 0.4$.

of width h and where $\alpha_2 = Q_2/(Q_1 + Q_2)$ is the volume fraction of the continuous phase [28]. In this type of system, as the void fraction $\alpha_1 = 1$–α_2 increases, the bubble length d_0 increases while the spacing L_0 decreases. In turn, this permits the formation of a range of dispersions from dilute suspensions with small bubbles to concentrated dispersions with large bubbles. For larger capillary numbers $\mathrm{Ca} \approx 1$, the lubricating film was shown to reach an average thickness on the order of $\delta/h \approx 10^{-1}$ for both low-viscosity droplets [29] and gas bubbles in thick oils [20]. In this situation, the size d_0 of deformable capillary objects is slightly enlarged compared to the previous scaling relationship due to the presence of a lubrication layer. However, as the increase in size d_0 is accompanied with a rise of bubbles or droplets spacing L_0 to conserve mass over a spatial period of the flow pattern, the linear aspect ratio of segmented flows in square microchannels was found to follow $L_0/d_0 \approx Q_2/Q_1$ from low to high Ca. Hence, the initial spacing-to-length ratio L_0/d_0 provides a useful reference to study the evolution of individual bubble shape and collective arrangement in nonlinear microgeometries.

We first examine the evolution of microfluidic multiphase flows by quantifying the evolution of the linear aspect ratio of segmented flows L/d in the modulated channel from low to high bubble concentration at large Ca [Fig. 2(a)]. Given the low value of $\mathrm{Re} < 10^{-1}$ investigated in this work, flows are fully developed with negligible entrance lengths and bubbles adopt a regular periodic behavior in the first corrugation. Hence, the transition region from straight to corrugated microgeometries allows for comparing the evolution of basic flow arrangements. Spatiotemporal analysis of bubble motion is conducted to extract both spatial and temporal evolution of the bubble length d and spacing L, which are initially constant in the square channel and referred to as d_0 and L_0 [Fig. 2(b)]. As a single bubble is strongly deformed due to a difference between its front and rear cap velocities in the corrugation, we examine the temporal evolution of a bubble of length d together with the spacing L from the next downstream bubble to associate a single reference time to these quantities as opposed to computing and assigning an average bubble-based reference point for the position. As a result of flow deceleration, d is found to decrease in the first part of the pore (i.e., for x/h ranging from 0 to 2) and

increase in the second part (i.e., for x/h between 2 and 4) due to convective acceleration. The initial bubble size is recovered at the constriction $d_{MAX} \approx d_0$ from small to moderate initial size $d_0/h \leqslant 2$. The relationship for L is more complex, as it represents the distance between the rear cap and the front cap of different bubbles at various locations. Data reveal, however, that the relation between L and d follows specific orbital trajectories over a cycle set with their magnitudes of modulation [Fig. 2(c)]. An effect of compaction on segmented flows due to corrugations is characterized with a short-time apparent contact between bubbles when $L/h \approx 0$. In this case, the viscous intercalating film between bubbles does not fully drain and no bubble coalescence is observed over the relatively short convective time scale investigated. Such apparent bubble contact typically introduces a long tail in the orbits prescribed in the (L, d) plane for large and concentrated bubbles [Fig. 2(c)(iii)].

The instantaneous evolution of the linear aspect ratio shows the existence of specific peaks $(L/d)_{MAX}$ that coincide with the maximum value of L since, in practice, the bubble spacing varies in larger proportions compared to d [Fig. 2(d)]. The dynamic maximum value $(L/d)_{MAX}$ is compared with the original aspect ratio and displays a scaling of the form $(L/d)_{MAX} \approx k(L_0/d_0)^{0.8}$ with the constant $k = 0.81$ [Fig. 2(e)]. This functional relationship characterizes the overall compressive effect of corrugations on the morphology of segmented flows along the bubble path. For dilute dispersions, $L_0/d_0 > 1$, the most important contributing factor to this phenomenon resides with the average reduction of the bubble spacing L compared to L_0, while for concentrated dispersions, $L_0/d_0 < 1$, bubbles crowded along the flow direction in a pore enlarge in the lateral direction w to allow for a reduction of d compared to d_0. The dynamic maximum of the aspect ratio $(L/d)_{MAX}$ is a useful parameter to classify flow regimes observed along the bubble flow path of the corrugated channel. The transition from compact to dilute segmented flow is characterized with $(L/d)_{MIN} \sim 0$, which corresponds to $(L/d)_{MAX} \approx 0.4$ [Fig. 2(e)]. A similar type of relationship was observed in much wider microfluidic chambers from the transition from single to multiple layer droplet arrangements [24].

IV. BUBBLE DEFORMATION AND CAPILLARY NUMBER

We now turn our attention to the effect of the capillary number Ca on the deformation of individual bubbles and on the shape of the bubble path, which can be defined by the envelope amplitude of the lateral bubble deformation w in the corrugation. The viscous nature of the flowing suspending liquid produces a strong dissymmetry on the bubble shape. Examples of bubbles passing through a constriction are presented in Fig. 3(a). At low capillary number $Ca \approx 10^{-2}$, bubbles adopt smoothly curved interfaces with round shapes that resemble those of a balloon, while for larger $Ca > 10^{-1}$, bubbles deform with sharp angles, suggesting the morphology of triangles where both front and rear caps display pointy shapes when oriented toward the accelerating flow and flatten edges when positioned toward the decelerating flow.

To investigate interfacial deformations in a pore, superimposed bubble contours at fixed intervals of time can be seen in Fig. 3(b). As expected, bubble edges follow nearly circular arcs in the chamber for low Ca, whereas straight end caps are found near the center of the chamber and conical shapes appear near the constriction for high Ca. The lateral amplitude of bubble deformation also delineates the effective bubble path in the complex geometry. In the limit of $Ca \approx 0$, the bubble path is symmetrical with respect to the flow direction due to the mirror shape of the pore. As Ca increases, however, a marked bulge appears in the region of the path located in the decelerating region of the pore [Fig. 3(b)]. During the high-Ca regime, graphical analysis of individual end caps is implemented using a time series of selected bubble contours. In particular, Fig. 3(c) shows the dynamics of rounded front menisci propagating in the throat as well as the retraction of the cusps formed by rear menisci. As for fixed periods of time, the distance between contours is proportional to interfacial velocity, Fig. 3(c) shows that a capillary pull exerted by the total area of a bubble during deformation induces important velocity variations on end caps, such as the occurrence of a fast tail retraction mechanism where the peak velocity is reached slightly upstream of the minimum pore width.

The spatial evolution of the lateral amplitude of deformation w is shown for various bubble sizes in Fig. 3(d). The location x_{MAX} where the maximal amplitude w_{MAX} is reached in the pore moves

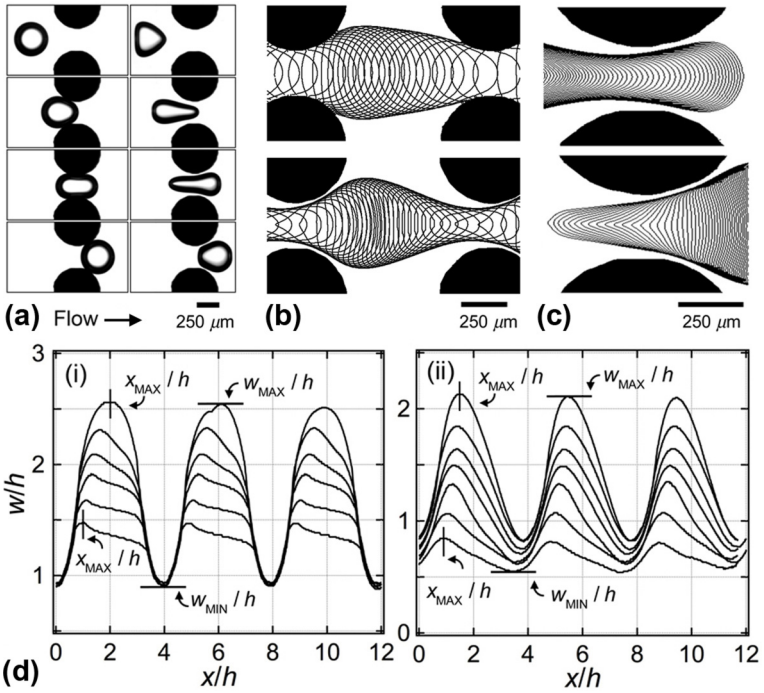

FIG. 3. Lateral deformation and bubble path in corrugated microchannels. (a) Time series of experimental micrographs showing bubbles passing through a constriction for low Ca $\approx 3.9 \times 10^{-2}$ with oil viscosity $\nu = 10^1$ cS (left) and high Ca $\approx 3.6 \times 10^{-1}$ with oil viscosity $\nu = 10^3$ cS (right). (b) Superimposition of bubble contour in a pore for low Ca $\approx 4.7 \times 10^{-2}$ ($\nu = 10^1$ cS, $\Delta t = 2.5 \times 10^{-3}$ s) (top), and high Ca $\approx 7.1 \times 10^{-1}$ ($\nu = 10^3$ cS, $\Delta t = 2.5 \times 10^{-3}$ s) (bottom). (c) Contour superimposition of front (top) and rear (bottom) bubble cap in a constriction, Ca $= 7.1 \times 10^{-1}$, $\Delta t = 5 \times 10^{-4}$ s. (d) Spatial evolution of lateral bubble amplitude w for various bubble sizes, (i) low Ca ranging between 2.7×10^{-2} and 7.7×10^{-2} ($\nu = 10^1$ cS), (ii) high Ca ranging between 2.9×10^{-1} and 7.1×10^{-1} ($\nu = 10^3$ cS).

downstream from the chamber entrance as the bubble size increases. For low Ca, the amplitude w_{MAX} remains relatively constant in the pore, while w rapidly decreases for large Ca to form a marked bulge in the bubble path in this regime. Similar to that of a straight channel, the film thickness between bubble and walls is relatively small for low Ca, which is recovered with a minimal amplitude $w_{\mathrm{MIN}} \approx h$ in the constriction. By contrast, this quantity is notably lower than the channel size for large Ca. The ratio $w_{\mathrm{MIN}}/w_{\mathrm{MAX}}$ corresponds to the critical interfacial curvature for the snap-off of long bubbles [30], here we show that for relatively small bubbles, this parameter also depends on bubble size and capillary number.

The mirror symmetry of our corrugations is useful for comparing the effect of converging and diverging microflows on bubble deformation from low to large capillary number Ca. As accelerating flows typically induce bubble elongations while decelerating streams produce lateral deformations, the bubble aspect ratio d/w experiences regular variations as bubbles pass through strings of pores and throats. The influence of the capillary number Ca on these deformations can be represented based on the local channel width $W_{\mathrm{C}}/h = 1 + 4\sin(x\pi/\lambda)^2$, where x is the location of the bubble centroid. Over a spatial period between ridges, the channel width varies between $W_{\mathrm{C}}/h = 1$ at the neck and $W_{\mathrm{C}}/h = 5$ at the center of the pore. In Fig. 4(a), the hysteretic paths of bubble deformation d/w along the local channel width W_{C}/h are shown for low and large capillary numbers. The range of variations in the amplitude of d/w between pores and throats and the large difference between convective paths delineates distinct hysteretic loops that grow in size with the capillary number Ca. To quantify this

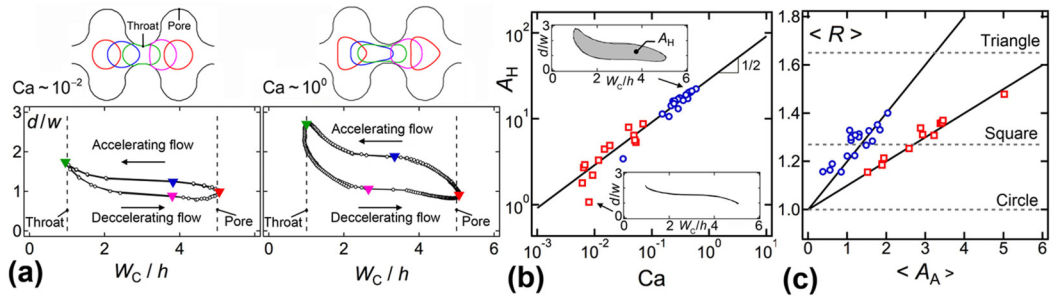

FIG. 4. Characterization of shape hysteresis of convected bubbles in corrugated channels. (a) Spatial evolution of bubble aspect ratio d/w as a function of channel width W_C/h for low and large capillary number Ca over a spatial period λ. (b) Influence of Ca on normalized hysteretic area A_H for low-viscosity $\nu = 10$ cS (□) and high-viscosity $\nu = 10^3$ cS (○) fluids, solid line: $A_H = 29\,\mathrm{Ca}^{1/2}$. (c) Evolution of average bubble roundness $\langle R\rangle$ as a function of mean bubble cross-sectional area $\langle A_A\rangle$; low-viscosity oil $\nu = 10$ cS (□) with solid line $\langle R\rangle = 1 + 0.1\langle A_A\rangle$ and high-viscosity oil $\nu = 10^3$ cS (○) with solid line $\langle R\rangle = 1 + 0.2\langle A_A\rangle$; dashed lines $\langle R\rangle = 1$ (circle), 1.27 (square), and 1.65 (equilateral triangle).

effect, we calculate the hysteretic area A_H comprised within the two curves in the $(d/w\text{-}W_C/h)$ space and find a scaling of the form $A_H \approx \mathrm{Ca}^{1/2}$ [Fig. 4(b)]. As the balance between shear and capillary stresses progressively shifts toward the viscous regime, bubble asymmetry between accelerating and decelerating flows becomes more marked. We find in particular that this trend is consistent over a few decades of variation in Ca and occurs for both low- and high-viscosity fluids. To further characterize bubble morphology, we calculate the apparent roundness $R = p_A^2/(4\pi A_A)$, where p_A and A_A are the respective cross-sectional perimeter and area of bubbles in the field of view. While the bubble area remains mostly constant as it progresses through the microchannel, the roundness undergoes significant variations, peaking at throats and reducing in pores. To assess bubble deformation throughout the corrugation, both the roundness and the apparent bubble area are averaged over one wavelength λ, leading to $\langle R\rangle$ and $\langle A_A\rangle$, respectively. Within the range of bubble size investigated here, we find that the roundness increases linearly with the bubble area [Fig. 4(c)]. Both low- and high-viscosity fluids exhibit a similar trend, but the high-viscosity case displays larger roundness values for similar areas, consistent with the observed bubbles' angular shapes.

V. BUBBLE PACKING

In this section, we examine the relationship between bubble deformation and geometrical arrangement of multiphase flows in varying geometries. In particular, morphological features of segmented flows are shown to strongly influence bubble deformation during the flow of concentrated bubble trains at large Ca. While injection of air and high-viscosity oil in the square microchannel produces bubble arrangements that are characterized with a small bubble size at low void fraction and large bubbles at higher concentration according to $L_0/d_0 \approx Q_2/Q_1$, the use of CO_2 gas permits the formation of additional multifluid arrangements. In this case, bubbles significantly collapse after the initial encapsulation with oil in the square channel and reach a uniform size upstream from the constriction. The absorption of carbon dioxide gas at the fluid interface during initial dissolution yields a reduction of d_0 while L_0 remains relatively constant [20], and regimes, such as bubbly flows, i.e., bubbles of subchannel size $d_0 < h$ as well as concentrated flows of small bubbles, become experimentally accessible.

Over the range of parameters investigated, measurements of the maximal lateral deformation w_{MAX} with respect to the bubble size d_{MAX} show the occurrence of symmetric deformations for small bubbles where lateral and longitudinal deformations are directly proportional, $w_{MAX} = d_{MAX}$ [Fig. 5(a)]. This regime is useful for microfluidic tensiometric tests [23]. For more concentrated

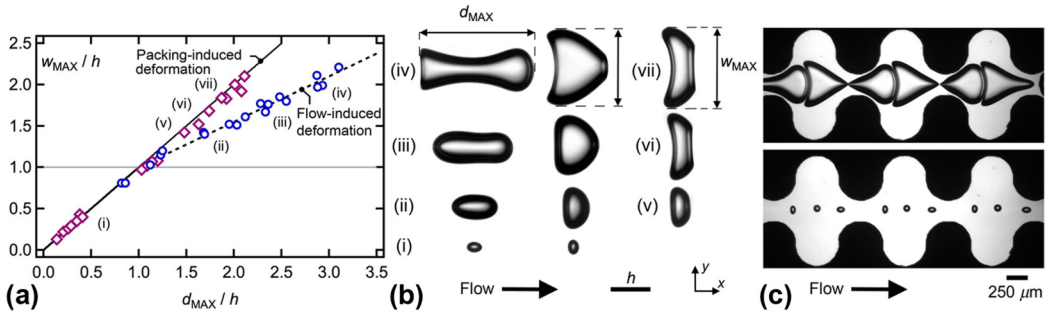

FIG. 5. Lateral and longitudinal amplitudes of bubble deformation at large Ca in corrugated, high-viscosity oil $\nu = 10^3$ cS. (a) Evolution of maximal width w_{MAX} as a function of length d_{MAX} for $\nu = 10^3$ cS from bubbly to segmented flows. Gas: air (○) or CO_2 (◇), solid black line: $w_{MAX} = d_{MAX}$, dashed line: $w_{MAX}/h = 0.55(d_{MAX}/h–1) + 1$. (b) Micrographs of maximal deformation, from (i) to (iv): dilute segmented flow (d_{MAX}, w_{MAX}); from (v) to (vii): packing-induced arrangement of bubble produce deformed oblate shapes. (c) Examples of flows at the corrugation scale.

segmented flows, the configuration of bubble packing in each pore leads to two types of distortions, which we refer to as flow-induced deformation for regular nondissolving bubbles made of air and packing-induced deformation for dissolving bubbles made of CO_2 [Fig. 5(b)]. Arrangements of nondissolving bubbles for $d_0/h > 1.5$ are characterized with bubbles adopting complex triangular shapes with an inverted rear curvature. The maximal bubble width w_{MAX} displays a reduced dependency with respect to d_{MAX} according to $w_{MAX}/h = 0.55(d_{MAX}/h–1) + 1$. When the bubble size d_0 reaches the characteristic length scale of variation for the velocity field, which corresponds to $\lambda/2 = 2h$ in the system, bubbles sworn into complex viscous flow fields remain primarily deformed along the flow direction. By contrast, when bubbles of comparable size reach the corrugation for dissolving flows, the initial bubble spacing L is much shorter than d_{MAX} and bubbles are aligned in compact chains and exert strong hydrodynamic interactions on one another. In particular, the limited spacing L between bubbles leads to larger lateral deformations w_{MAX} compared to flow-induced distortions, and packing-induced deformation displays a direct correspondence between deformation and size according to $w_{MAX} = d_{MAX}$. The existence of two distinct packing behaviors observed in the same geometry illustrates the importance of both phase concentration and spatial distribution in multifluid dynamics. Examples of the wide variation in the scale of multiphase flows covered with these parameters are displayed in Fig. 5(c).

VI. BUBBLE VELOCITY

Finally, we examine the relationship between front and rear bubble velocities V_F and V_R with respect to the initial bubble velocity in the square channel V_0 [Fig. 6(a)]. The spatial evolution of the instantaneous front and rear bubble velocities are normalized with V_0 and show peak values in the constriction for the front meniscus and in the convergence for the rear cap, as previously evidenced with the observation of the cusp retraction associated with the capillary pull. Overall, the effect of surface tension is to reduce the maximal front velocity $V_{F,MAX}$ to limit bubble elongation and to increase the rear velocity $V_{R,MAX}$ in the convergence to facilitate bubble retraction. As a result, V_F is slightly lower than V_0, while V_R surpasses this reference value. We find that the arithmetic mean of the front and rear maximal velocities $V_B = (V_{F,MAX} + V_{R,MAX})/2$ is within a few percentiles of the initial velocity V_0 over a range of bubble size [Fig. 6(b)]. Therefore, V_B provides a useful intrinsic parameter for comparison with the average bubble velocity in a pore defined as $V_A = \lambda/T$, where T is the period of bubble transport across each pore. Besides differences in rear and front velocities, the time period T remains the same for each bubble meniscus. Data show that the average bubble velocity in a pore is relatively large, $V_A \approx 0.5V_B$ [Fig. 6(c)]. This remarkable effect is related to

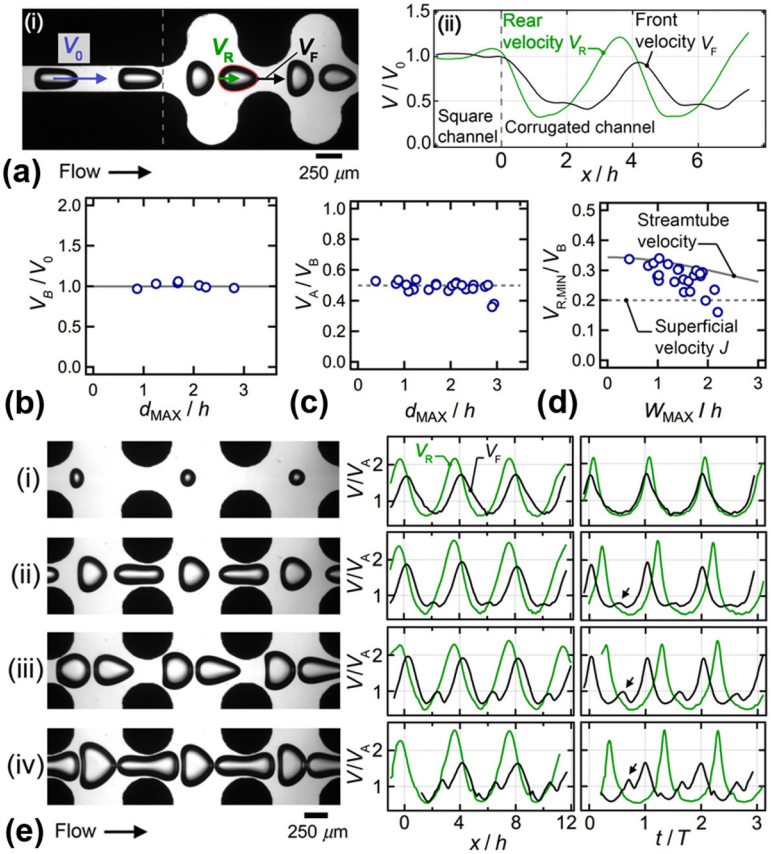

FIG. 6. Bubble velocity variation. (a) Example of evolution of front and rear bubble velocities V_F and V_R in a series of pores. (b) Mean of maximal velocities is identical to initial velocity, $V_B \approx V_0$ for a range of bubble size d_{Max}. (c) Comparison of V_B and V_A for various bubble sizes, solid line: $V_B/V_A = 0.5$. (d) Evolution of minimal rear bubble velocity $V_{R,\,Min}$ as a function of maximal lateral deformation w_{Max}. (e) Effect of bubble size of front and rear velocity evolution, Ca ranges between 2.3×10^{-1} and 3.8×10^{-1}.

the presence of thick lubricating films near the channel walls at large Ca and the location of the bubble path in the center of the corrugation. Indeed, in the limit of large Ca, bubbles are bounded within a central stream tube of width w_{MAX} that does not experience as much deceleration in the middle of the pore as the average superficial velocity of the multiphase flow $J = 0.2V_B$, which is based on a simple mass conservation argument. To highlight this property, we plot the minimal rear bubble velocity measured in the pore V_{MIN} normalized with V_B as a function of the maximal lateral deformation w_{MAX} [Fig. 6(d)]. Data show that the minimal velocity V_{MIN} is bounded between J and the computed average velocity of a stream tube of width w_{MAX}.

The flow of deformable capillary objects in a corrugation at large Ca produces complex dynamics based on a combination of individual bubble deformations and collective distortions of segmented flows. Examples of spatiotemporal analyses of bubble velocities of various sizes and arrangements are displayed in Fig. 6(e). The spatial evolutions of V_F and V_R show that curves are shifted for small d and synchronized for large d, while the temporal evolution shows the opposite trend, i.e., a synchronized behavior for small d and curves that are out of phase for large bubbles. In both cases when $d > h$, the front velocity V_F shows a nonmonotonic behavior with the presence of a second velocity peak that becomes more prominent as the bubble size increases. This effect is attributed to the finite size of bubbles having a front cap in the converging flow and a rear cap in the diverging

flow of a pore. The temporal evolution of velocities suggests that while the front velocity is about to increase, the rear velocity decreases in such a way that it affects the front velocity and the convective acceleration of the front becomes dominated by the deceleration at the rear. As expected, this effect is relatively negligible for bubbles having sizes that are small compared to typical flow features, $d < h$. In summary, the effect of the capillary pull on bubbles is nontrivial, since in a constriction the bubble front pulls to the rear to produce large rear cusp velocities, while in a pore, the bubbles rear pull on the front end cap to make it decelerate.

VII. CONCLUSIONS

In this study, we examine individual deformation and collective motion of bubbles suspended in a complex viscous flow field at large capillary numbers. Corrugated microchannels with well-defined geometries are used to distort trains of bubbles that are regularly produced in a hydrodynamic focusing section. While segmented flows in straight channels are characterized with a fixed bubble size d_0 and spacing L_0, the presence of cavities along the corrugated microchannel produces large periodic variations of these quantities. We show in particular that bubbles follow specific orbital trajectories in the (L, d) space in corrugated microchannels. Analysis of the instantaneous ratio L/d also reveals the existence of a maximal value that follows a simple scaling relationship based on initial conditions. The critical initial aspect ratio for initiating a bubble apparent contact is also examined. To better understand the influence of the capillary number on bubble deformation, the lateral envelope amplitude of individual bubbles is computed from experimental data. Lateral deformation of bubbles delineates the shape of flow paths that are closely related to the capillary number. We then show that the hysteresis in the shape of a bubble between accelerating and decelerating flow fields increases with the capillary number Ca. For concentrated bubble trains, we identify flow-induced and packing-induced deformations. Finally, detailed analysis of bubble velocity reveals the influence of a capillary pull, where the finite size of bubbles alters the velocities of front and rear menisci, including a nonmonotonic behavior for the front velocity in a smooth pore.

Overall, the proposed system provides a simple model of porous media through a succession of throats and pores representing interstices and cracks. Physical measurements of bubble behavior in specific geometries offer useful reference for validating numerical experiments of multiphase flows in a variety of microgeometries. The morphological evolution of segmented flows provides an important metric to quantify viscous effects during the flow assembly of bubbles in periodically constricted capillaries. While the progressive symmetry breaking in the bubble shape along the flow direction was previously observed from low to large capillary numbers in straight channels, our study clarifies the influence of convective extensional flows on bubble deformation. In particular, flow field variations near the front and rear end caps of bubbles lead to the formation of capillary number gradients that significantly alter local interfacial curvatures in a fashion suggesting dynamic Marangoni effects. While no surfactant was used in this study, experimental, numerical, or theoretical extensions of this work could include investigations into the relationships between longitudinal and lateral bubble distortions as well as bubble spacing in the presence of tensioactive substances and non-Newtonian fluids in nonlinear geometries.

ACKNOWLEDGMENT

This material is based upon work supported by the National Science Foundation under Grant No. CBET-1150389.

[1] B. Legait, Laminar flow of two phases through a capillary tube with variable cross-section, J. Colloid Int. Sci. **96**, 28 (1983).

[2] T. C. Ransohoff and C. J. Radke, Weeping flow around nonwetting bubbles trapped in constricted noncircular pores, PhysicoChem. Hydrodyn. **8**, 255 (1987).

[3] T. C. Ransohoff, P. A. Gauglitz, and C. J. Radke, Snap-off of gas bubbles in smoothly constricted noncircular capillaries, AIChE J. **33**, 753 (1987).

[4] A. Z. Zinchenko and R. H. Davis, Motion of deformable drops through porous media, Annu. Rev. Fluid Mech. **49**, 71 (2017).
[5] J. C. Magniez, M. Baudoin, C. Liu, and F. Zoueshtiagh, Dynamics of liquid plugs in prewetted capillary tubes: From acceleration and rupture to deceleration and airway obstruction, Soft Matter **12**, 8710 (2016).
[6] C. R. Carrigan and J. C. Eichelberger, Zoning of magmas by viscosity in volcanic conduits, Nature (London) **343**, 248 (1990).
[7] N. I. Gershenzon, R. W. Ritzi, Jr., D. F. Dominic, E. Mehnert, and R. T. Okwen, Capillary trapping of CO_2 in heterogeneous reservoirs during the injection period, Int. J. Greenhouse Gas Cont. **59**, 13 (2017).
[8] M. jiang, K. Budzan, and G. Drazer, Fractionation by shape in deterministic lateral displacement microfluidic devices, Microfluid Nanofluid **19**, 427 (2015).
[9] E. Brouzes, A. Carniol, T. Bakowski, and H. H. Strey, Precise pooling and dispensing of microfluidic droplets toward micro- to macro-world interfacing, RSC Adv. **4**, 38542 (2014).
[10] M. Prakash and N. Gershenfeld, Microfluidic bubble logic, Science **315**, 832 (2007).
[11] F. P. Bertherton, The motion of bubbles in tubes, J. Fluid Mech. **10**, 166 (1961).
[12] H. Wong, C. J. Radke, and S. Morris, The motion of long bubbles in polygonal capillaries, Part 1. Thins films, J. Fluid Mech. **292**, 71 (1995).
[13] C. H. Shih and L. J. Lee, Analysis of void removal in liquid composite molding using microflow models, Polym. Compos. **23**, 120 (2002).
[14] G. Dawson, E. Haner, and A. Juel, Extreme deformation of capsules and bubbles flowing through a localised constriction, Procedia IUTAM **16**, 22 (2015).
[15] W. L. Olbricht and L. G. Leal, The creeping motion of immiscible drops through a converging/diverging tube, J. Fluid Mech. **134**, 329 (1983).
[16] D. R. Graham and J. J. L. Higdon, Oscillatory flow of droplets in capillary tubes, Part 2. Constricted tubes, J. Fluid Mech. **425**, 55 (2000).
[17] M. Pailha, A. L. Hazel, P. A. Glendinning, and A. Juel, Oscillatory bubbles induced by geometrical constraint, Phys. Fluids **24**, 021702 (2012).
[18] S. L. Anna, Droplets and bubbles in microfluidic devices, Annu. Rev. Fluid Mech. **48**, 285 (2016).
[19] T. Fu and Y. Ma, Bubble formation and breakup dynamics in microfluidic devices: A review, Chem. Eng. Sci. **135**, 343 (2015).
[20] M. Sauzade and T. Cubaud, Initial microfluidic dissolution regime of CO_2 bubbles in viscous oils, Phys. Rev. E **88**, 051001(R) (2013).
[21] D. R. Link, S. L. Anna, D. A. Weitz, and H. A. Stone, Geometrically Mediated Breakup of Drops in Microfluidic Devices, Phys. Rev. Lett. **92**, 054503 (2004).
[22] T. Cubaud, D. Henderson, and X. Hu, Separation of highly viscous fluid threads in branching microchannels, Microfluid Nanofluid **20**, 55 (2016).
[23] J. T. Cabral and S. D. Hudson, Microfluidic approach for rapid multicomponent interfacial tensiometry, Lab Chip **6**, 427 (2006).
[24] B. M. Jose and T. Cubaud, Droplet arrangement and coalescence in diverging/converging microchannels, Microfluid. Nanofluid. **12**, 687 (2012).
[25] M. Sauzade and T. Cubaud, Bubbles in complex microgeometries at large capillary numbers, Phys. Fluids **26**, 091109 (2014).
[26] W. L. Olbricht and D. M. Kung, The deformation and breakup of liquid drops in low Reynolds number flow through a capillary, Phys. Fluids A **4**, 1347 (1992).
[27] M. J. Madou, *Fundamentals of Macrofabrication and Nanotechnology* (CRC Press, Boca Raton, FL, 2012), Vol. II.
[28] R. Sun and T. Cubaud, Dissolution of carbon dioxide bubbles and microfluidic multiphase flows, Lab Chip **11**, 2924 (2011).
[29] B. M. Jose and T. Cubaud, Formation and dynamics of partially wetting droplets in square microchannels, RSC Adv. **4**, 14962 (2014).
[30] A. R. Kovcek and C. J. Radke, Gas bubble snap-off under pressure-driven flow in constricted noncircular capillaries, Colloids Surf., A **117**, 55 (1996).